

The Modeling of Transverse Solids Motion in Rotary Kilns

H. HENEIN, J. K. BRIMACOMBE, and A. P. WATKINSON

Mathematical models have been developed to predict the conditions giving rise to the different forms of transverse bed motion in a rotary cylinder: slumping, rolling, slipping, cascading, cataracting, and centrifuging. Model predictions of the boundaries between these modes of bed motion compare well with previously reported measurements, and can be represented conveniently on a Bed Behavior Diagram which is a plot of pct fill against Froude number (or bed depth vs rotational speed). The location of the boundaries is shown to depend on material variables which characterize frictional conditions in the bed. For the slumping/rolling boundary these are primarily the shear angle and the limiting wedge angle which defines the solids involved in a slump. For the slipping/slumping and slipping/rolling boundaries the governing material variables are the bed/wall friction angle and the upper angle of repose and dynamic angle of repose, respectively. Similarly, the location of the other boundaries related to cascading and cataracting is determined by the dynamic angle of repose. Complete Bed Behavior Diagrams have been calculated for solids having different particle size and particle shape rotated in cylinders having different diameters.

I. INTRODUCTION

THE representation of transverse solids motion in a rotary kiln by a Bed Behavior Diagram (plot of bed depth vs rotational speed or percent fill vs Froude number) has been described in a previous paper.¹ Experimentally it was shown that the boundary between slumping and rolling beds in this diagram was a function of particle size, particle shape, static angle of repose, kiln diameter, rotational speed, and local bed depth in a rotary kiln. This study also revealed that the slumping/rolling boundary of given granular solids could be determined only from the boundary of another material by comparing their static angles of repose, their slumping frequencies, or by applying the scale-up criteria:

$$[\text{Fr}]_M \left[\frac{D}{d_p} \right]_M^{1/2} = [\text{Fr}]_P \left[\frac{D}{d_p} \right]_P^{1/2}$$

and

$$(\text{pct fill})_M = (\text{pct fill})_P$$

The purpose of this paper is to provide a fundamental basis for the slumping/rolling behavior of solids beds as well as for the other modes of bed motion—slipping, cascading, cataracting, and centrifuging—in a rotary cylinder. The analysis to be described makes it possible to predict bed behavior quantitatively from measured particle characteristics and the bed/wall friction coefficients.

II. PREVIOUS WORK

Modeling of transverse solids flow in rotary cylinders previously has focused on the characterization of the thickness of the active layer on the bed surface, the rate and

extent of transverse mixing and, using rigid-body mechanics, the conditions for slipping and centrifuging at the kiln wall. The active-layer thickness has been described mathematically for a rolling or a cascading bed,^{2,3} but owing to the complex nature of particle kinematics in real systems, the models are of limited use for predictive purposes. The primary aim of the mixing studies³⁻¹² was to develop, using statistical techniques or diffusion analogies, a coefficient of mixedness by which the mixed or unmixed state of the solids could be evaluated. Many of these coefficients have been proposed, but none has found wide application. Carley-Macaulay and Donald^{5,6} and Hogg³ have studied transverse mixing of cascading solids and shown that transverse mixing is at least two orders of magnitude faster than axial mixing. Their results as well as those of Lehmberg *et al*⁴ indicate that the mixing kinetics are first order. However, using these modeling approaches little insight is gained on the mechanisms involved or on the influence of many of the material, operating, and design variables of the system. The solids mechanics approach to bed-behavior modeling has been attempted for a slipping bed. For rotary-kiln applications the three forces to be accounted for are: gravitational, frictional, and centrifugal. Many different points of application and magnitudes of these forces have been proposed,^{13,21} yet no fully satisfactory solution for the slipping bed is available. This modeling approach has also been applied to predict centrifuging.

III. MODEL DESCRIPTION

A. The Slumping/Rolling Boundary

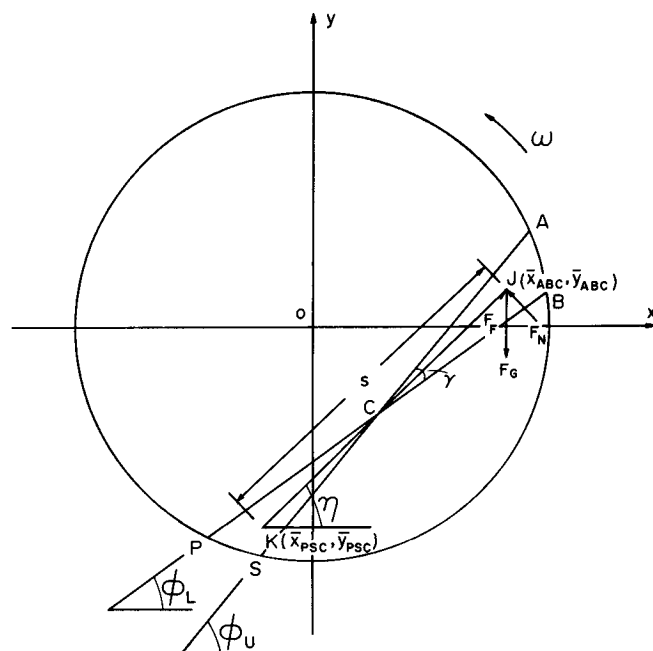
Before developing the model to predict the change from slumping to rolling beds it is worthwhile to examine the various processes occurring within a slump cycle. As the solids rotate with the cylinder wall the friction force between particles varies between zero and some limiting value. Due to the nature of bulk solids, the internal stress distribution is not uniform in the bed and is indeterminate until the limiting condition of friction is attained when a shear plane is formed (the bulk solids lying above the shear plane will be termed

H. HENEIN, formerly Graduate Student, Department of Metallurgical Engineering, University of British Columbia, is now with the Department of Metallurgical Engineering and Materials Science, Carnegie-Mellon University, Pittsburgh, PA 15213 as Assistant Professor. J. K. BRIMACOMBE, Stelco Professor of Process Metallurgy, Department of Metallurgical Engineering, and A. P. WATKINSON, Professor, Department of Chemical Engineering, are both with The University of British Columbia, Vancouver, British Columbia V6T 1W5, Canada.

Manuscript submitted October 8, 1982.

The trajectory of each of the particles in the shear wedge (ABC, Figure 1) could be determined from one of the three principles of solids flow, the minimization of energy. However, since there is no information on the manner in which the potential energy of the solids is dissipated, a trajectory model has been developed in this study based on the conversion of the potential energy of the particles in the shear wedge solely to kinetic energy as they fall from wedge ABC to PSC (Figure 1). Their average trajectory then is given by the straight line joining the centroids of the two wedges. The resultant force on the shear wedge acts through its centroid and is given by

$$M \frac{d^2 S}{dt^2} = F_G \sin \eta - F_F \quad [1]$$

$$F_G = Mg \quad [2]$$
$$F_F = \mu_I F_N \quad [3]$$
$$F_N = Mg \cos \eta \quad [4]$$
$$\frac{d^2s}{dt^2} = g(\sin \eta - \mu_L \cos \eta) \quad [5]$$
$$\mu_L = \tan \phi_L \quad [6]$$


Integrating Eq. [5] with the initial conditions,

$$(i) \quad t = 0 \quad v = 0 \quad [7]$$

(ii) $t = 0$ $s = 0$ [8]

$$s = \frac{1}{\gamma} g t^2 (\sin \eta - \tan \phi_L \cos \eta) \quad [9]$$
$$S = [(\bar{x}_{ABC} - \bar{x}_{PSC})^2 + (\bar{y}_{ABC} - \bar{y}_{PSC})^2]^{1/2} \quad [10]$$
$$\eta = \tan^{-1} \left[\frac{\bar{y}_{ABC} - \bar{y}_{PSC}}{\bar{x}_{ABC} - \bar{x}_{PSC}} \right] \quad [11]$$
$$\gamma = \gamma_0 + 6C_1 n \quad [12]$$

The criterion governing the transition from a slumping to a rolling bed has been determined based on the extent of filling of the shear wedge by the upward rotating bed during the time taken for a slump, calculated from Eq. [9]. Over the time of downward motion of the shear wedge, the angular rotation of the bed is

$$\gamma^* = 6nt \quad [13]$$

$$t_0 = \frac{30}{\pi} \left(\frac{\gamma_0}{\omega} \right) \quad [14]$$
$$s = \left(\frac{450g}{\pi^2} \right) \left(\frac{\gamma_0}{\omega} \right)^2 (\sin \eta - \tan \phi_L \cos \eta) \quad [15]$$

Table I. Summary of Results for the Particle Characterization of the Materials Tested

Material	Average Size (mm)	Particle Shape	Particle Density (kg/m ³)	Loose Bulk Density (kg/m ³)	Dense Bulk Density (kg/m ³)	Loose Void Fraction	Dense Void Fraction	Static Angle of Repose (Deg)	Dynamic Angle of Repose (Deg)	Cylinder Diameter (m)	Shear Angle (Deg)
Gravel	3.0	Angular	2870	1560	1690	0.46	0.41	40.7	37.5	0.40	34.7
									37.0	1.06	34.4
Iron Oxide	11.6	Spherical	—	—	—	—	—	31.5	35.2	0.40	33.3
Limestone B	4.3	Irregular	2700	1450	1610	0.46	0.40	40.3	39.6	0.40	37.7
									36.5	1.06	34.5
Limestone C	1.5	Irregular	2690	1520	1600	0.43	0.40	37.8	36.0	0.40	33.6
										1.06	32.5
Limestone D	0.58	Irregular	2680	1490	1570	0.44	0.41	35.6	34.9	0.40	33.5
Limestone F	8.1	Angular	2690	—	—	—	—	42.8	41.5	1.06	38.5
Nickle Oxide	4.9	Spherical	—	870	900	—	—	32.5	30.2	0.40	29.9
Sand B	0.50	Nodular	2660	1640	1740	0.38	0.35	33.4	33.6	0.40	32.2

Table II. Dimensions of Rotary Vessels

Vessel	Inside Diameter (m)	Length (m)
Cylinder A	0.4	0.46
Cylinder B	0.4	0.86
Cylinder C	1.06	0.41

Table III. Regression Coefficients Obtained from the Sensor Data

Material	Cylinder Diameter (m)	Limiting Wedge Angle, γ_0 (Deg)	Dilatancy Coefficient, $C_1(s)$	Number of Observations
Gravel	0.4	5.00	0.536	58
Gravel	1.06	4.63	0.699	33
Iron Oxide	0.4	4.73	0.722	15
Limestone B	0.4	5.19	0.491	15
Limestone B	1.06	5.67	0.487	32
Limestone C	0.4	6.47	0.158	44
Limestone C	1.06	6.58	0.153	28
Limestone D	0.4	4.68	0.103	63
Limestone F	1.06	5.50	0.770	24
Nickel Oxide	0.4	2.94	0.614	30
Sand B	0.4	2.16	0.364	40

Also substituting,

$$\omega = \frac{v}{R} \quad [16]$$

and dividing by s , Eq. [15] becomes,

$$1 - \frac{1}{2} \left(\frac{gR}{v^2} \right) \left(\frac{R}{s} \right) \left(\frac{900\gamma_0^2}{\pi^2} \right) (\sin \eta - \tan \phi_L \cos \eta) = 0 \quad [17]$$

This equation is therefore the dimensionless form of the criterion for the slumping/rolling boundary and provides the scale-up criteria for the material, the cylinder, and the operating variables. The first dimensionless parameter, (gR/v^2) , is recognized as the inverse of the Froude number which is the ratio of the inertial to gravitational forces. The second scale-up factor, (R/s) , reflects the effect of pct filling as well as the size of the shear wedge. Thus, it is an operating as

well as a material scale-up factor. The third, $(900\gamma_0^2/\pi^2)$, represents a material variable, the minimum shear wedge; while the last parameter, $(\sin \eta - \tan \phi_L \cos \eta)$, is dependent on the fill ratio, the size of the shear wedge, the shear angle, and the cylinder diameter. For a given material and cylinder, only the first two dimensionless parameters (gR/v^2) and (R/s) may vary, and their values are solely a function of rotational speed and bed depth. Hence, the plotting of bed depth (pct fill) vs rotational speed (or Froude number) to delineate the slumping/rolling boundary described earlier is justified mathematically.

B. The Slipping Model

Uggla¹⁴ and Reuter¹⁹ both performed force balances on a rolling bed to predict conditions where slipping and rolling would occur. Their approach is unsatisfactory since all the forces involved are not coincident. Cross²¹ derived a model based on a differential moment analysis on a static bed. His result is unusual in that both the normal force and the anticlockwise moment appear independent of the inclination of the bed.

Here an improved model is developed to predict slipping conditions in a rotary kiln based on the principles of mechanics for rigid bodies. A bed of bulk solids rotated with the cylinder wall and having an angle of inclination, ϕ' , is considered as shown in Figure 2. The gravity force and the centrifugal force act through the center of gravity of the bed whose location is given by,

$$R_B = \frac{2R^3 \sin^3 \lambda}{3A} \quad [18]$$

where the area of the bed may be calculated from,

$$A = \frac{R^2}{2} (2\lambda - \sin 2\lambda) \quad [19]$$

The gravity force is given by Eq. [2] and the centrifugal force by,

$$F_C = M^2 \omega R_B \quad [20]$$

The resultant force is therefore,

$$F_R = (F_C^2 + 2F_C F_G \cos \phi' + F_G^2)^{1/2} \quad [21]$$

The moment balance about the center of rotation of the cylinder yields,

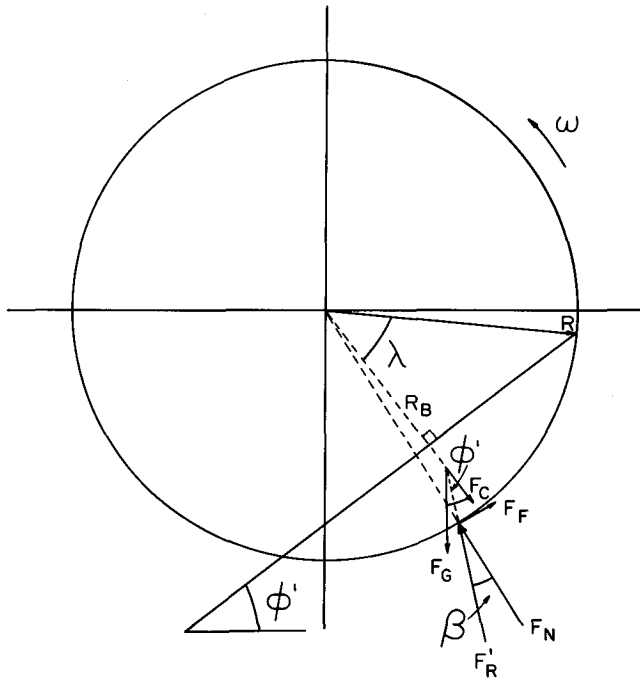


Fig. 2—Force balance on the bed of bulk solids for the slipping model.

$$F_F = \frac{R_B}{R} F_G \sin \phi' \quad [22]$$

In order for the forces to be in equilibrium (*i.e.*, no slipping at the wall) the normal and frictional forces also must have a resultant, F'_R , which is equal in magnitude but opposite in direction to F_R . Therefore,

$$F_F = F'_R \sin \beta \quad [23]$$

and

$$F_N = F'_R \cos \beta \quad [24]$$

It is known that the maximum frictional force is given by,

$$F_F = \mu_{w/s} F_N \quad [25]$$

and that,

$$\mu_{w/s} = \tan \phi_s \quad [26]$$

Therefore, substituting Eqs. [21] into [24] and [26] into [25] yields,

$$\tan \phi_s = \frac{\frac{R_B}{R} F_G \sin \phi'}{(F_C^2 + 2F_C F_G \cos \phi' + F_G^2)^{1/2} \cos \left\{ \sin^{-1} \left[\frac{\frac{R_B}{R} F_G \sin \phi'}{(F_C^2 + 2F_C F_G \cos \phi' + F_G^2)^{1/2}} \right] \right\}} \quad [27]$$

Equation [27] can be solved by trial and error for the resultant bed inclination, ϕ' , which then can be compared to the upper angle of repose, ϕ_U , and the resultant dynamic angle of inclination ϕ'_D , to be described in the following section. Three situations may arise,

$$(i) \phi' > \phi_U > \phi'_D$$

$$(ii) \phi_U > \phi' > \phi'_D$$

and

$$(iii) \phi_U > \phi_D > \phi'$$

In the first situation, no slipping occurs; while in the second, slipping occurs rather than slumping and finally, slipping replaces all other modes of bed behavior. For rolling beds the analysis can be simplified by comparing ϕ' to ϕ_D . Furthermore, when the centrifugal force is negligible, as in most rotary kilns, Eq. [27] simplifies to:

$$\tan \phi' = \frac{3 \tan \phi_s (\lambda - \cos \lambda \sin \lambda)}{2 \sin^3 \lambda} \quad [28]$$

This result appears more logical than that of Cross,²¹ in that the tangent of the inclination angle of the bed rather than the sine appears as the left-hand side of the equation. Slipping in rotary kilns is therefore a function of the slip angle, ϕ_s , and the pct fill. The results of the slipping model therefore may be plotted on a Bed Behavior Diagram.

C. The Cascading and Cataracting Models

Prediction of the onset of cascading and cataracting in rotary cylinders thus far has received little attention in the literature. Cascading has been identified previously by the crescent shape of the bed while cataracting has been characterized by a significant portion of granular solids being projected into the free space of the cylinder and showering back to the bed. Davis²³ and Ugla¹⁴ have attempted to calculate the onset of cataracting based on a force balance on a single particle resting on the surface of the bed. Davis did not account for the friction force and based his calculation on a cylinder having a fill ratio of 0.5. Ugla accounted for the friction force by using a static angle of friction.

For the current model, the force balance is carried out at the centroid of the bed shown in Figure 3(a) with the angle of kinetic friction equal to the dynamic angle of repose. The force balance yields,

$$+ \swarrow F_G \sin \phi'_D - F_F = 0 \quad [29]$$

$$+ \searrow F_N - F_C - F_G \cos \phi'_D = 0 \quad [30]$$

finally,

$$F_F = \mu_D F_N \quad [31]$$

Substituting for the appropriate terms and simplifying,

$$(\sin \phi'_D - \mu_D \cos \phi'_D) = \frac{\mu_D \omega^2 R_D}{g} \quad [32]$$

where,

$$\mu_D = \tan \phi_D \quad [33]$$

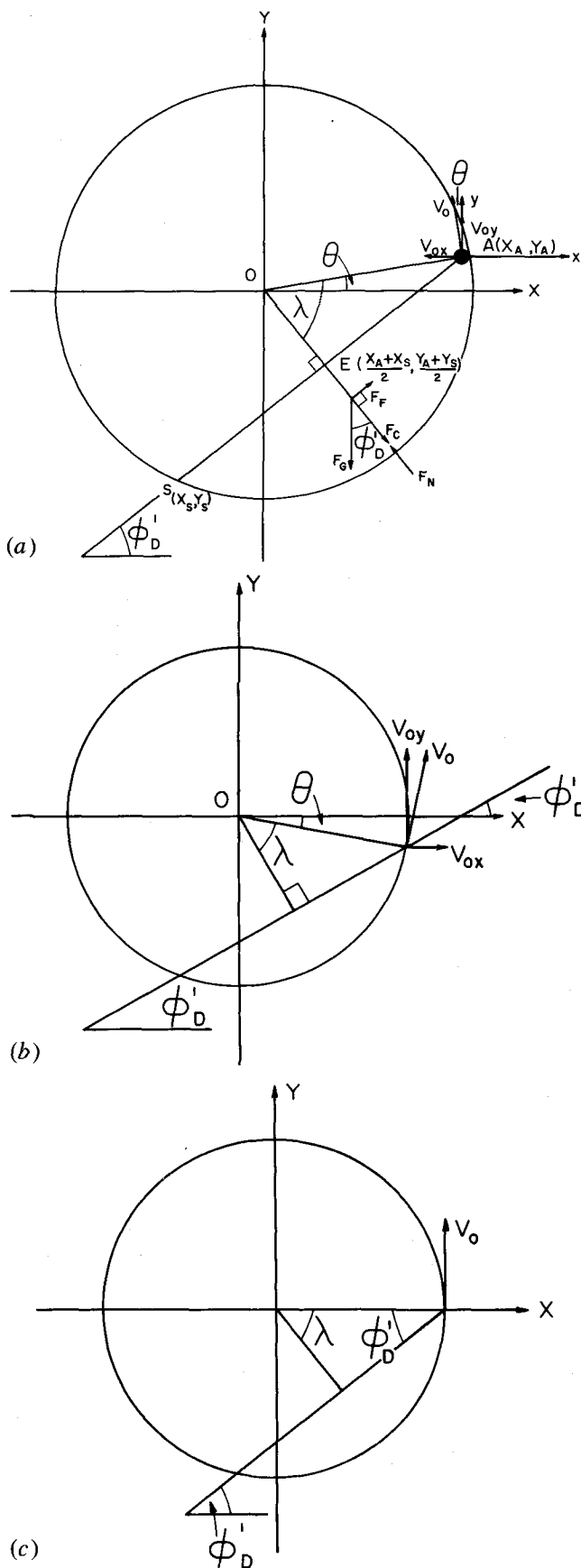


Fig. 3—(a) Force balance on the bed of bulk solids for the cascading model with the apex in the first quadrant. (b) Bed configuration with the apex in the fourth quadrant. (c) Bed configuration defining the rolling/cascading boundary.

Hence, the bed inclination for which the forces acting on the bed are in equilibrium can be calculated by trial and error from Eq. [32] which also can be simplified to,

$$\sin(\phi'_D - \phi_D) = \omega^2 R_B \sin \phi_D \quad [34]$$

or

$$\sin(\phi'_D - \phi_D) = \frac{\omega^2 R}{g} \left[\frac{2 \sin^3 \lambda}{3(\lambda - \cos \lambda \sin \lambda)} \right] \sin \phi_D \quad [35]$$

The resultant bed inclination, ϕ'_D , is therefore a function of the Froude number, the pct fill, and the dynamic angle of repose.

When the resultant bed inclination, ϕ'_D , places the apex of the bed in the fourth quadrant, the outermost particle at the cylinder wall has an initial velocity into the wall (Figure 3(b)), and the angle θ is negative. However, once the resultant bed inclination places the apex in the first quadrant, the velocity of the outermost particle is away from the wall and the particle is projected into the open space of the cylinder (Figure 3(a)). This has been defined as cascading. Note that in this configuration the angle θ is positive. The rolling/cascading boundary therefore is defined by the rotational speed giving a resultant bed inclination, ϕ'_D , which places the apex of the bed on the abscissa as illustrated on Figure 3(c). In this configuration,

$$\theta = 0 \quad [36]$$

and

$$\lambda = 90 - \phi'_D \quad [37]$$

Substituting Eq. [37] into Eq. [35] and simplifying yields,

$$\frac{\omega_{R/c}^2 R}{g} = \frac{3}{2} \left[\frac{\tan \phi'_D}{\mu_D} - 1 \right] \left[\frac{\left[\frac{\pi}{2} - \phi'_D \right]}{\cos^2 \phi'_D} - \tan \phi'_D \right] \quad [38]$$

Equation [38] reveals that the rolling/cascading boundary is a function of the cylinder size, the dynamic angle of repose of the solids, the rotational speed, and the pct fill. Hence, the rolling/cascading boundary may be described on a Bed Behavior Diagram.

The cascading/catacting boundary is based on the criterion that particles projected from the apex of the bed fall to, or beyond, the midpoint of the bed surface. In the ensuing analysis, a parabolic trajectory is assumed for the particles, and interactions between particles in flight have been neglected.^{23,24} The inclination of the bed has been calculated from Eq. [35]. The parabolic trajectory of the uppermost particle on the bed surface is given by,

$$Y = R \sin \theta - \frac{(R \cos \theta - X)}{\tan \theta} + \frac{g(R \cos \theta - X)^2}{2v_0^2 \sin^2 \theta} \quad [39]$$

where

$$X = R \sin \theta - \left[\frac{2v_0^2 \sin \theta}{g} \right] \left[\cos \theta + \sqrt{\frac{Rg}{v_0^2} \sin \theta - \sin^2 \theta} \right] \quad [40]$$

and

$$v_0 = \omega R \quad [41]$$

The coordinates of the midpoint of the bed surface (Figure 3) are given by,

$$X_E = (R - H) \cos(\theta - \lambda) \quad [42]$$

and

$$Y_E = (R - H) \sin(\theta - \lambda) \quad [43]$$

From the above equations it is seen that, as with the rolling/cascading boundary, the cascading/catacting boundary is dependent on the cylinder diameter, the dynamic angle of repose of the material, the rotational speed, and the pct fill.

D. Centrifuging

The critical rotational speed at which a particle at the cylinder wall centrifuges can be calculated from the following equation:

$$n_c = \frac{30}{\pi} \sqrt{\frac{2g}{D}} \quad [44]$$

The Froude number at the initiation of centrifuging is unity.

Thus, the complete transverse bed behavior for a given material, showing the various areas of predominance of slipping, slumping, rolling, cascading, catacting, and centrifuging, may be predicted and represented on a Bed Behavior Diagram given the following input variables:

- [i] the radius of the cylinder, R ,
- [ii] the limiting angle of the shear wedge, γ_0 ,
- [iii] the wedge angle as a function of rotational speed, γ_0 and C_1 ,
- [iv] the shear angle, ϕ_L ,
- [v] the dynamic angle of repose, ϕ_D , and
- [vi] the bed/wall friction angle, ϕ_S .

IV. MODEL PREDICTIONS AND DISCUSSION

A. The Slumping/Rolling Boundary

The characterization of the materials and the dimensions of the rotary vessels used in this study have been described

in a previous paper¹ and are listed in Tables I and II, respectively. The predicted and experimental slumping/rolling boundaries for Limestone B tested in Cylinders A and B are shown in Figure 4. The determination of the experimental boundaries have been previously described¹ while the boundary predictions were obtained using the model already presented in this paper. The maximum and minimum values of γ_0 and C_1 were calculated for 95 pct confidence limits and were used to obtain the upper and lower limits of the slumping/rolling boundary, also plotted in Figure 4. This essentially yields the error in the predictions of the slumping/rolling boundaries from the measurements of γ_0 and C_1 . Thus, for Limestone B, the variation in γ_0 of ± 0.3 deg and in C_1 of ± 0.1 s result in a change in the predicted boundary of about ± 0.15 and ± 0.25 rpm, respectively, for the upper and lower confidence limits of the coefficients. This is of the same order as the width of the experimentally determined transition zone. Good agreement is observed between predicted and experimental boundaries, particularly with respect to the bed depth dependency.

Bed depth influences the slumping/rolling boundary because for a given cylinder diameter it determines the distance separating the centroids of the shear wedge (other factors affecting wedge geometry such as the wedge angle are independent of bed depth (Appendix A)). Thus, raising the bed depth increases the distance and time of travel of the solids between the upper and lower centroids of the shear wedge (ABC and PSC in Figure 1). At equal rotational speeds, the angular distance traveled by the cylinder during the collapse of the shear wedge is then greater and the time available to refill the shear wedge is increased. The result is a greater tendency for rolling with increased bed depths. This also can be seen from Eq. [15].

The slumping/rolling boundary predicted by the model for solids with a more spherical shape than the irregular Limestone B is shown in Figure 5. The solids are nickel oxide spheres having roughly the same particle size (4.9 mm) as Limestone B (4.3 mm, Table I). The model predictions, which agree well with measurements made in Cylinder A also shown in Figure 5, indicate that the nickel oxide bed begins to roll at a considerably lower rotational

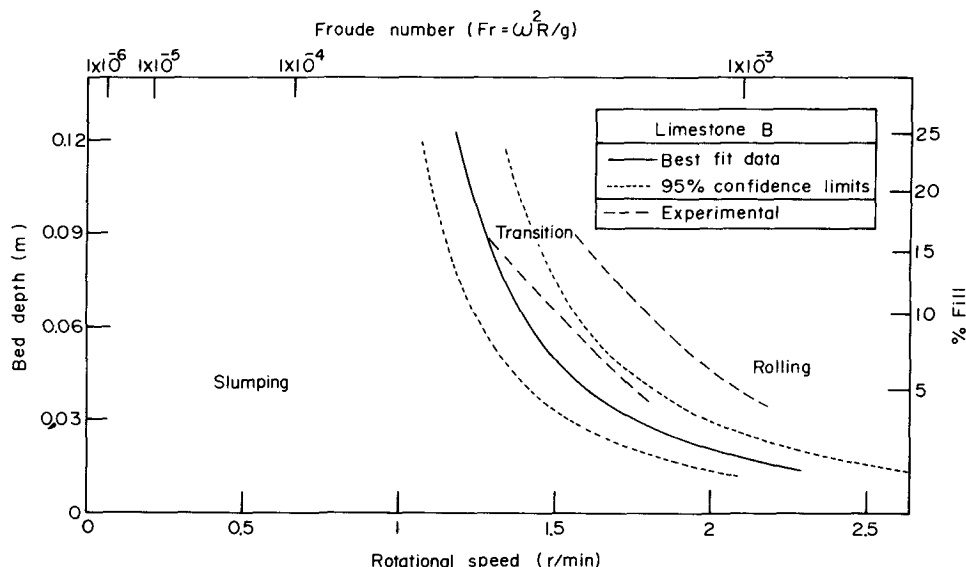


Fig. 4—Predicted and experimental slumping/rolling boundaries for Limestone B tested in Cylinders A and B (0.4 m ID \times 0.46 m L and 0.86 m L, respectively).

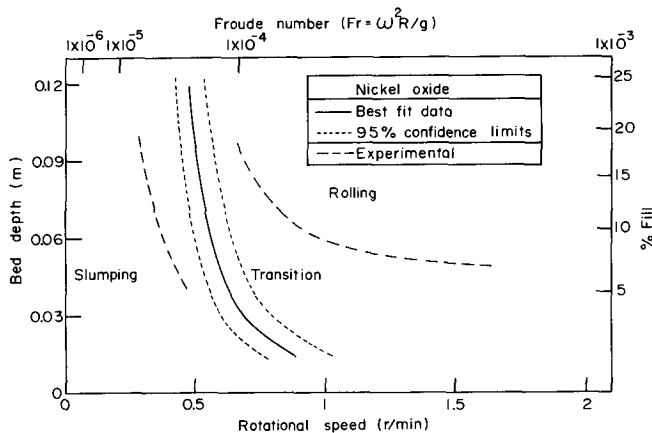


Fig. 5—Predicted and experimental slumping/rolling boundaries for nickel oxide tested in Cylinder A (0.4 m ID \times 0.46 m L).

speed than Limestone B (Figure 4). The reason for this effect is best seen by examining Eq. [15], the values of the shear angle, Table I, and limiting wedge angle, Table III, measured for the two materials.* The shear angle of nickel

*Strictly, the dilatancy coefficient, C_1 , should also be considered, but its effect on γ over the range of rotational speeds of interest is small.

oxide, 29.9 deg, is lower compared to 37.7 deg for Limestone B, and the limiting wedge angle, 2.94 deg, is also smaller relative to 5.19 deg for Limestone B. The smaller angles for the nickel oxide will result in a negligible effect on the values for s , but will give a reduced value for the term $(\sin \eta - \tan \phi_L \cos \eta)$ in Eq. [17]. Coupled with the reduced value of γ_0 , lower rotational speeds clearly are necessary to achieve rolling for the nickel oxide particles. Expressed differently, the smaller shear wedge of nickel oxide particles can be filled in a shorter time and hence the rotational speed required to achieve rolling ($\gamma^* = \gamma_0$)

is lower than for Limestone B. From Eq. [17] the scaling criteria for particle shape is therefore $[(900\gamma_0^2)/\pi^2]$ and $(\sin \eta - \tan \phi_L \cos \eta)$.

The same effect of particle shape is observed with beds of smaller particles. The predicted and measured slumping/rolling boundaries for Limestone D (0.58 mm, irregular) and Sand B (0.50 mm, nodular) are shown in Figures 6 and 7, respectively. Again, the model correctly predicts that the nodular Sand B rolls at lower rotational speeds than the irregular Limestone B for the reasons cited above. In addition, the slumping/rolling boundary predicted by the model for the irregular particles is more dependent on bed depth than for nodular or spherical particles. This conforms broadly with the measurements of slumping/rolling.

The influence of particle size is seen by comparing the slumping/rolling boundaries predicted for Limestone B (4.3 mm) and D (0.58 mm) in Figures 4 and 6, respectively. Thus, the bed of smaller particles rolls at a lower rotational speed. From Tables I and III the shear angle and minimum wedge angle are shallower for the smaller particle size which is consistent with the arguments developed earlier for particle shape. Furthermore, the scaling criteria already presented for particle shape can be used to predict the boundary of one material from that of the other when comparing bulk solids with different sizes and shapes.

The slumping/rolling boundary also has been predicted for Limestone B in a larger cylinder, Cylinder C (Table II), with an ID of 1.06 m. Note that all previous calculations have been made for cylinders having an ID of 0.4 m. The predicted and measured slumping/rolling boundaries for this case are presented in Figure 8. It is seen that with greater pct filling, the predicted boundary is located at higher rotational speeds than the experimental boundary, and the latter exhibits a greater dependence on bed depth. The reason for the difference is not clear, particularly in view of the good agreement obtained for the other cases.

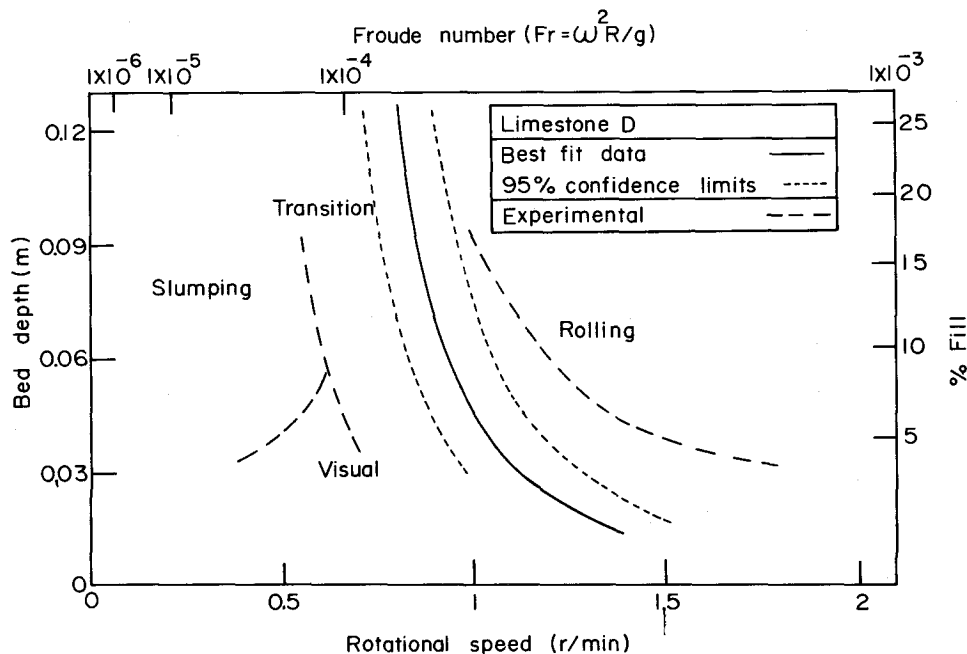


Fig. 6—Predicted and experimental slumping/rolling boundaries for Limestone D tested in Cylinder A (0.4 m ID \times 0.46 m L).

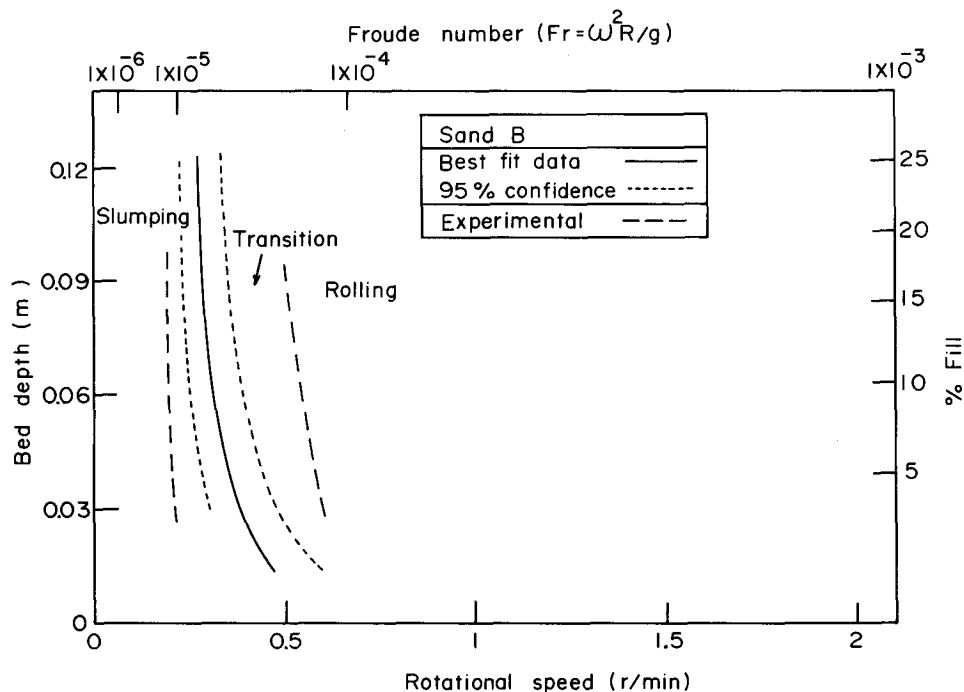


Fig. 7—Predicted and experimental slumping/rolling boundaries for Sand B tested in Cylinder A (0.4 m ID \times 0.46 m L).

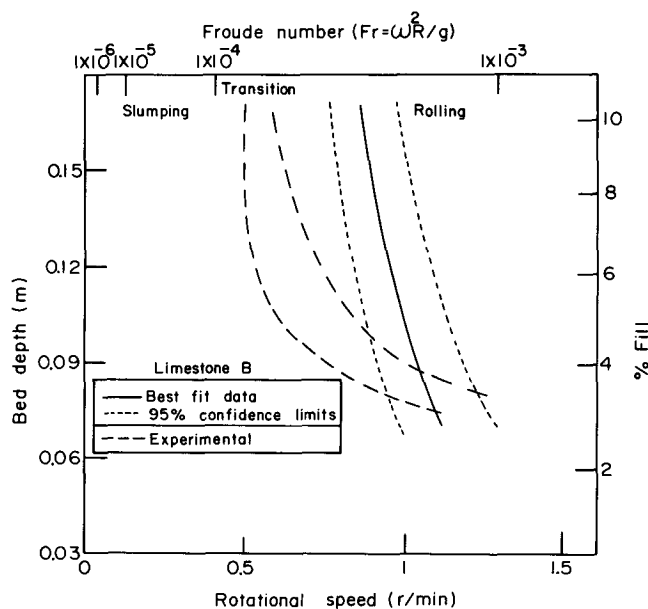


Fig. 8—Predicted and experimental slumping/rolling boundaries for Limestone B tested in Cylinder C (1.06 m ID \times 0.4 m L).

B. Slipping

The predictions of the slipping model presented earlier are shown in Figure 9 as a plot of the resultant bed inclination, ϕ' , against the bed/wall friction (slipping) angle, ϕ_s . ϕ' has been calculated for three levels of Froude number, kiln diameters from 0.4 to 2.7 m, and pct filling from 1 to 25. Note that the model predictions for the different kiln diameters are identical at the same values of slip angle, pct fill, and Froude number. The curves shown in Figure 9 delineate regions of slipping (below the plots) and no slipping (above the plots).

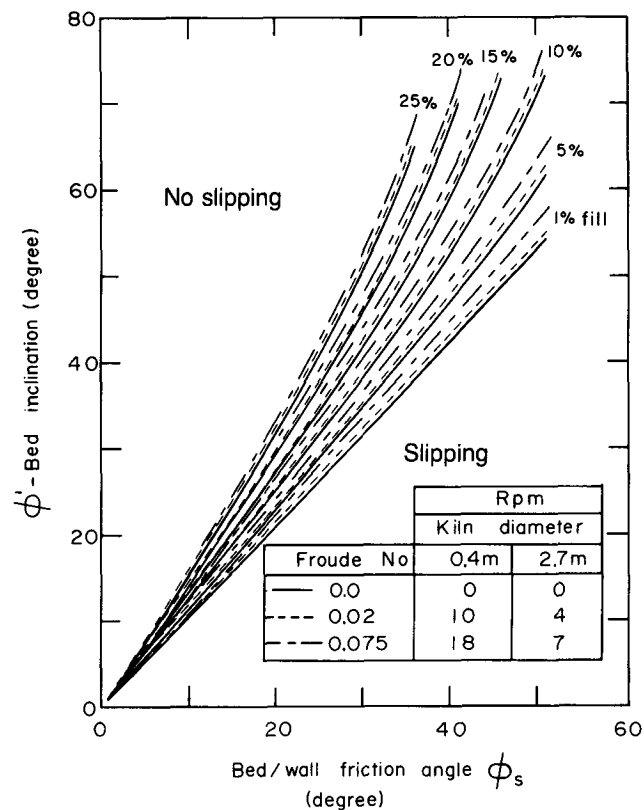


Fig. 9—Predictions of the slipping model for kiln diameters of 0.4 to 2.7 m.

This can be seen, as stated earlier, by comparing the resultant bed inclination at slipping, ϕ' , to the upper angle of repose, ϕ_u , if slumping dominates under nonslip conditions or the dynamic angle of repose, ϕ_d , if the bed tends to roll.

Thus, for example, if at a given bed/wall friction angle, ϕ_s , and pct fill, ϕ' , is less than ϕ_U , the bed will slip against the wall without slumping. If at constant ϕ_s the pct filling is raised, the bed will continue to slip until ϕ' has increased to a value equal to ϕ_U , at which point the bed will begin to slump. A similar argument could be made for the slumping-rolling transition.

This illustration shows that the pct filling of the bed is a key variable affecting slipping, and that slipping is enhanced by a low solids loading in a rotary kiln. Examination of the curves in Figure 9 reveals an equally important finding with respect to rotational speed. For a given pct fill and bed/wall friction angle, rotational speed has a negligible influence on ϕ' and hence on slipping. This finding has been substantiated by industrial observations of ball mills.^{26,27,28}

From this analysis it is clear that to avoid slipping in rotary kilns, only two variables can be effectively manipulated: the bed/wall friction angle and the pct fill. The rotational speed will not change slipping except under special conditions which will be discussed in the next section. In kiln operations the bed/wall friction angle may be increased to prevent slipping by roughening the wall. This may be effected in a number of ways. Refractory bricks of different heights can be installed in a staggered array to provide small ledges protruding from the kiln lining. Internal devices such as mixers will have a similar result.²⁹ Some lime producers roughen the refractory wall by feeding salt to the kiln, but this has the concomitant effect of decreasing the reactivity of the lime subsequently produced.^{30,31} Methods of increasing the pct loading of the kiln to prevent slipping include raising the feed rate, lowering the kiln inclination, decreasing the rotational speed, raising the height of end dams,

or installing dams within the kiln to control the axial loading profile. Of these, the installation of new dams or modification of existing dams may be the most practicable.

Finally, it should be noted that the pct fill may change through the kiln owing to the formation of accretions, and the bed/wall friction angle also may vary. Thus, depending on local conditions, the bed may be slipping in one zone (often the back end of the kiln), slumping in another, and rolling in yet another zone. The interrelationship of these different modes of bed motion is best seen on a Bed Behavior Diagram which is presented in the next section.

C. The Complete Bed Behavior Diagram

All six modes of bed behavior, predicted with the models formulated in this study, are shown in Bed Behavior Diagrams in Figures 10 to 13 for four of the cases seen in Table I. Shown also are the measured slumping/rolling boundaries for each case. Slipping was not observed in the measurements because the bed/wall friction angle always was greater than the static and dynamic angles of repose. Had the cylinder wall been smoother, however, with, say $\phi_s = 30$ or 35 deg, the slipping boundary would have occurred as indicated in Figures 10 to 13 by the horizontal lines below which slipping predominates. As the bed/wall friction angle decreases, *i.e.*, smoother walls, the area on the diagram dominated by slipping increases. As shown in the previous section, the rotational speed has a negligible effect on the slipping boundaries which are influenced solely by the bed/wall friction angle and pct fill. Note that for the same value of ϕ_s , the slipping/slumping boundary is found at a higher pct fill than either the slipping/rolling or slipping/

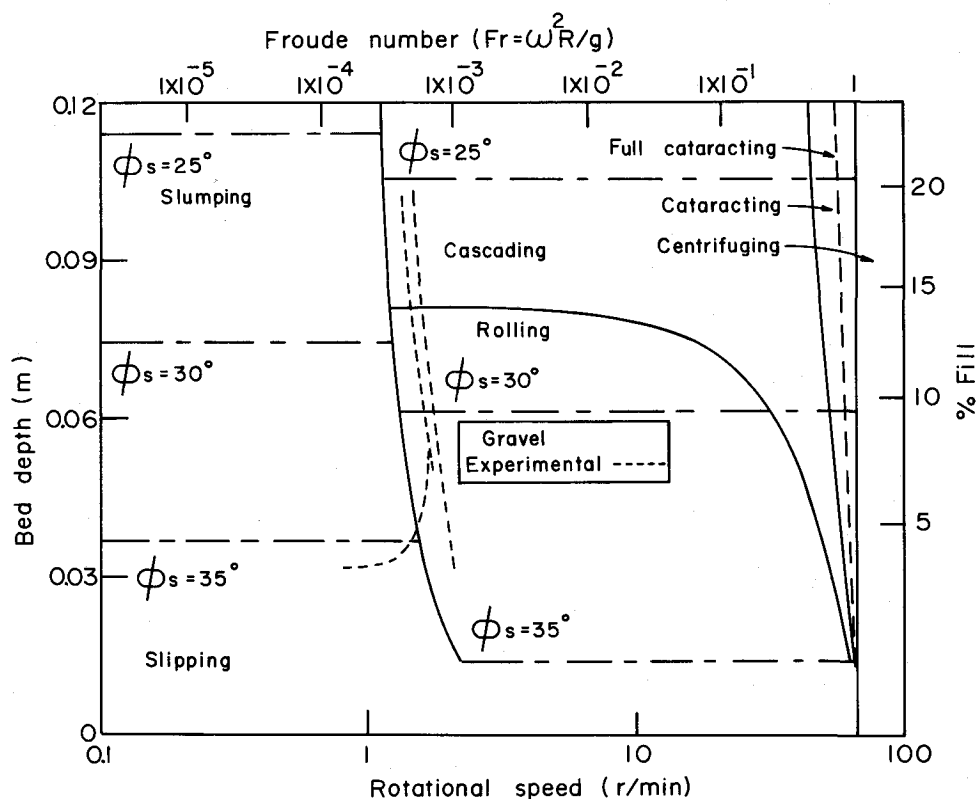


Fig. 10—Complete Bed Behavior Diagram of gravel in Cylinder A (0.4 m ID \times 0.46 m L).

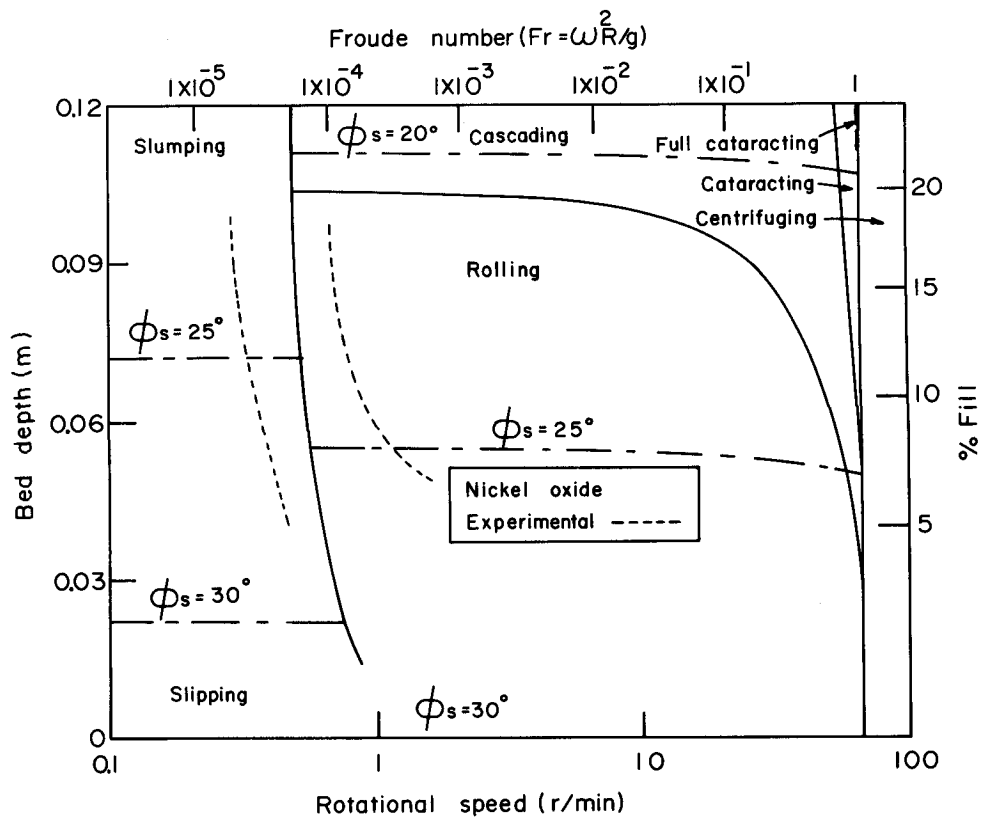


Fig. 11—Complete Bed Behavior Diagram of nickel oxide in Cylinder A (0.4 m ID \times 0.46 m L).

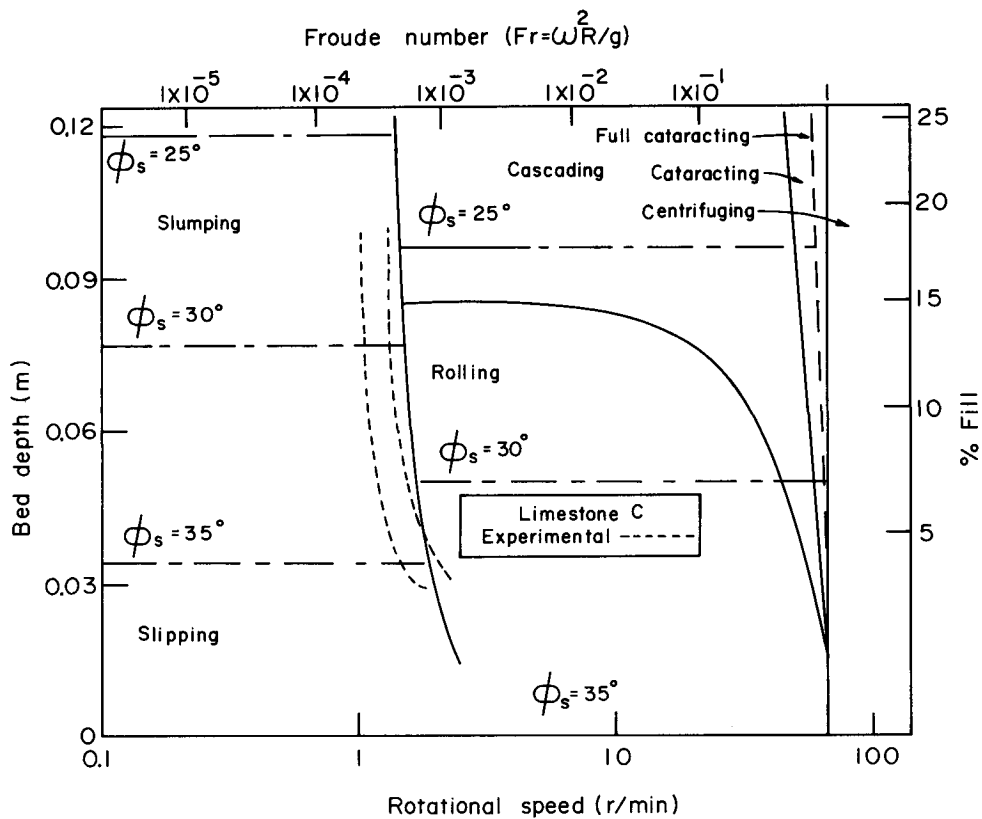


Fig. 12—Complete Bed Behavior Diagram of Limestone C in Cylinder A (0.4 m ID \times 0.46 m L).

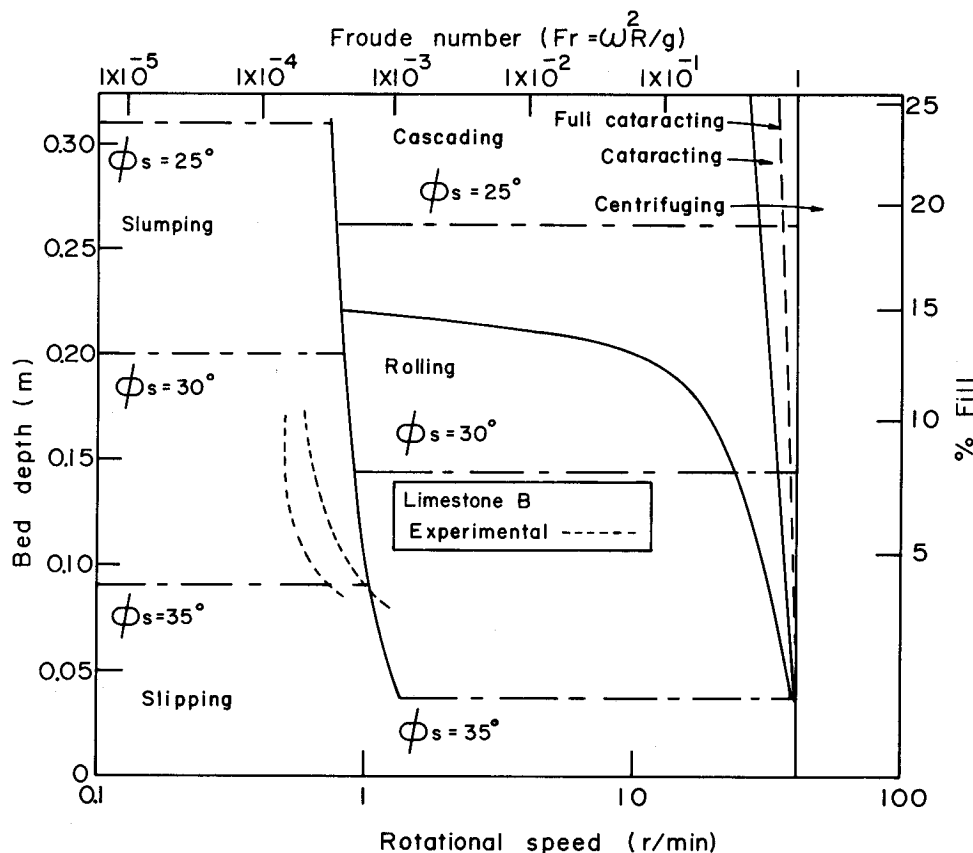


Fig. 13—Complete Bed Behavior Diagram of Limestone B in Cylinder C (1.06 m ID \times 0.4 m L).

cascading boundaries. This is due to the dynamic angle of repose being lower than the static angle of repose.¹

The criteria proposed in this paper for slipping are in agreement with the experimental and industrial observations of other workers. The experiments of Rose and Blunt³² on ball mills showed that the Froude number was not an important scaling criterion for slipping. The negligible effect of rotational speed on slipping was also observed by Korotich³³ using a cylinder, 0.3 m ID, rotating between 10 to 65 rpm (Froude numbers from 0.02 to 0.71). The charge in the cylinder slipped over the full range of rotational speeds at all solids loadings up to 20 pct whereupon slipping ceased. The observations of Gow *et al.*²⁸ and Duda²⁷ on ball mills are also similar. In rotary kilns, Ronco¹⁵ observed slipping to cease with increasing pct fill. Lehmberg *et al.*⁴ observed slipping at 2 rpm but, by increasing the rotational speed to 5 rpm, slipping stopped and rolling set in. With a rougher cylinder wall or a higher static angle of repose of the solids, these workers may otherwise have observed slumping at 2 rpm. By increasing the rotational speed to 5 rpm, the slumping/rolling boundary was crossed and the solids were observed to roll, since the slipping/rolling boundary probably occurred at lower pct loadings than the slipping/slumping boundary. Finally, it should be mentioned that the (D/d_p) scale-up ratio proposed by Rose and Blunt³² for slipping is likely incorporated in the measured value of ϕ_s used as an input to the slipping model.

At higher solids loadings in Figures 10 to 13, rolling is absent and slumping changes directly to cascading. This

follows from the definition of cascading given earlier and results in the occurrence of a triple point between slumping, rolling, and cascading, the position of which is a function of the dynamic angle of repose. The triple point of materials with a lower dynamic angle of repose, such as nickel oxide ($\phi_D = 30.2$ deg) shown in Figure 11, is located at higher values of pct loading. Similarly, comparing Figure 11 to Figures 10 and 12, it is evident that the cascading/cataracting boundaries for materials with a lower value of ϕ_D (Table I) are situated at higher Froude numbers. The full cataracting line on the Bed Behavior Diagrams represents the rotational speed at which the parabolic trajectory of the outermost particle leaving the apex of the bed intersects the cylinder wall at the base of the bed.

The effect of cylinder diameter can be seen by comparing Figures 12 and 13. It should be noted that the dynamic angle of repose of Limestone C in Cylinder A is 36 deg while that for Limestone B in Cylinder C is 36.5 deg. Moreover, the ratio of (D/d_p) for the two cases also is nearly identical. As discussed in an earlier paper,¹ this ratio is important in the scale-up of the slumping/rolling boundary. Comparing Figures 12 and 13, the boundaries delineating slumping, rolling, cascading, cataracting, and centrifuging are found in the same positions relative to Froude number and pct filling. From this it would seem that the scaling criteria for cascading and cataracting are also the Froude number and the pct fill as well as the dynamic angle of repose rather than the angle of detachment of particles which has been suggested in the literature.^{14,23}

Predictions of cascading and cataracting in this work agree with previously reported findings. Cataracting has been observed to occur at Froude numbers in the range of 0.25 to 0.72^{26,34,35} which is in agreement with the model predictions shown in Figures 10 to 13. The speed of the particles falling down the slope of the bed is reported by Muller³⁶ to depend on the slope of the bed, and hence cascading is a function of the dynamic angle of repose as shown in this study. Finally, Oyama⁷ has presented the following empirical relationship for predicting the cascading/ataracting and the full cataracting boundaries,

$$n = \frac{K}{D^{0.47} f^{0.14}} \quad [45]$$

where K is a constant equal to 54 for the cascading/ataracting boundary and 72 for the full cataracting condition. Although Oyama has not accounted for the dynamic angle of repose, the boundaries predicted using Eq. [45] agree to within ± 15 pct of the rotational speeds predicted with the models presented in this paper. The cascading and cataracting predictions are therefore reliable.

From this discussion it is clear that with the exception of centrifuging, each mode of solids motion is characterized by four independent parameters: a material variable (the frictional behavior of the solids), a system variable (the pct fill), and two external forces acting on the bed (the gravity and centrifugal forces). Thus, it is logical to map these types of solids motion on the same figure, as has been done in this work.

On a final note, some caution should be exercised in applying the Bed Behavior Diagrams based on cold solids measurements to high-temperature rotary-kiln operations. Rapid evolution of gas from the bed, physical changes to the solids as they travel through the kiln (changes in coefficients of friction, or angles of repose with temperature or reaction, degradation or agglomeration), or the formation of wall accretions can influence bed behavior in the real system in a way not seen in the Bed Behavior Diagrams. With some difficulty, these phenomena could be taken into account. For example, in the case of rapid gas evolution, a third force, drag, could be included in the Bed Behavior Diagrams. In the case of solids degradation different Bed Behavior Diagrams would be necessary to characterize solids motion in different zones of the kiln. High temperature measurements also may be required to assess the effect of agglomeration and accretion formation on bed behavior.

V. SUMMARY

A semi-empirical model has been formulated to predict the change in bed motion from slumping to rolling in a rotary kiln. Model predictions of the slumping/rolling boundary compare favorably with measurements involving solids of different particle size and particle shape rotated in cylinders having different diameters. From this study, scaling criteria were found to be the Froude number, pct fill, and the limiting wedge angle which defines the solids involved in a slump.

Slipping, cascading, and cataracting bed motion also have been mathematically modeled; and model predictions are in agreement with experimental observations reported

in the literature. It is shown that slipping is influenced primarily by the pct fill of the bed and the bed/wall friction angle while rotational speed has a negligible effect. Cascading and cataracting are determined by the pct fill, Froude number, and the dynamic angle of repose of the bed.

The six modes of bed motion have been represented on a Bed Behavior Diagram for different solids rotated in cylinders of different size.

APPENDIX A

Characterization of a slump

The shear angle or lower angle of repose, ϕ_L , and wedge angle, γ , of slumping beds were determined for the materials shown in Table I using rotary cylinders having a plexiglas end-plate (Table II). The latter measurements were made both photographically using a HYCAM motion-picture camera and with infrared sensors.²² The motion pictures of slumping were taken at 40 fps with both the plexiglas end-plate and a mirror reflection of the surface of the solids bed in the field of view. The cinematography revealed that the solids on the bed surface moved prior to the angle of inclination of the bed reaching a maximum³⁶ as the solids in the shear wedge assumed a denser packing. Comparison of photographic observations of successive slumps with oscillating signals recorded from the infrared sensors showed that maxima and minima in the signals correspond to the upper and lower angles of repose, respectively. Thus, the wedge angle can be determined conveniently from the time between a minimum and a maximum, t_1 , as follows:

$$\gamma_1 = 6\pi t_1 \quad [A.1]$$

Agreement between values of t_1 measured photographically and with the sensors was very good.

The times to maximum and minimum bed inclinations, t_1 and t_2 , respectively, were measured for different bed depths and rotational speeds for the different materials seen in Table I. A typical set of results is presented graphically for gravel in Figure A.1, where each point represents an average of at least 25 measurements (for clarity of presentation not all points are included in the diagram). Both times, t_1 and t_2 , were observed to be independent of bed depth for all materials tested in the cylinders described in Table II. The form of the equation used for regression on the t_1 data was,

$$t_1 = \frac{\gamma_{01}}{6 \cdot n} + C_1 \quad [A.2]$$

Multiplying both sides of Eq. [A.2] by $(6 \cdot n)$ yields,

$$\gamma_1 = \gamma_{01} + 6 \cdot C_1 \cdot n \quad [A.3]$$

The size of the shear wedge is therefore equal to a constant, the minimum shear wedge, γ_{01} , plus the rotational speed times a time constant, C_1 , when dilatancy is believed to occur and will be referred to as the dilatancy coefficient. For time t_2 , the following equation was used:

$$t_2 = \frac{\gamma_{02}}{6 \cdot n} + C_2 + C_3 n \quad [A.4]$$

A simple regression was performed on the t_1 data and a standard multiple regression on the t_2 data. The minimum wedge angle is then

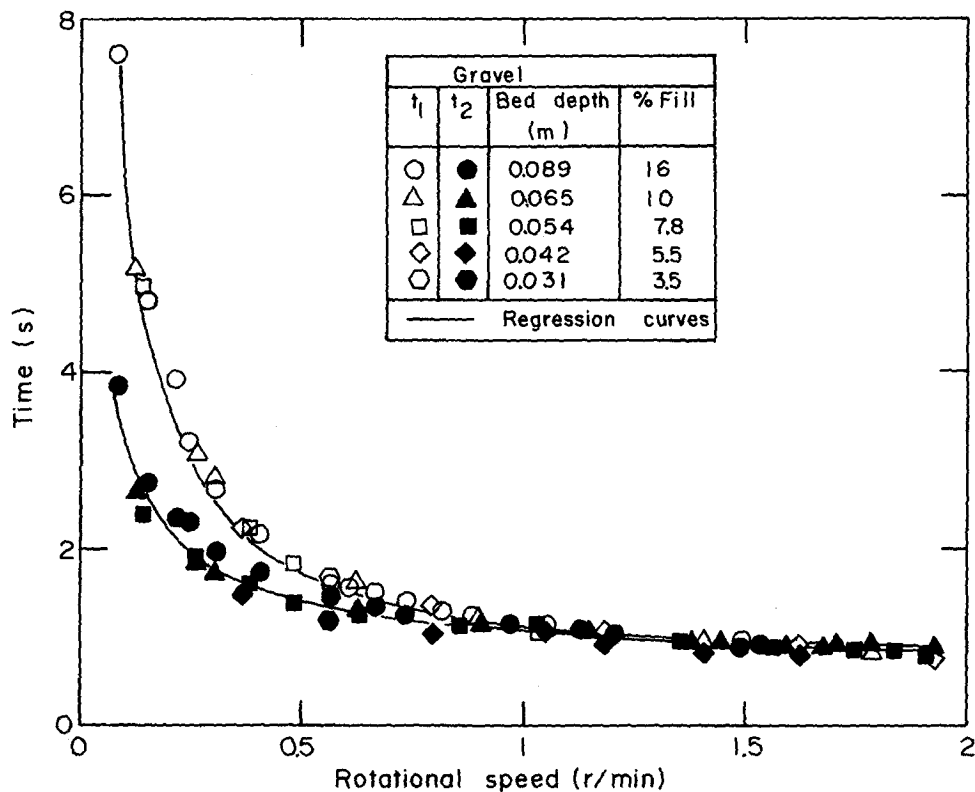


Fig. A.1—The t_1 and t_2 measured results as well as the regression curves for gravel in cylinder A (0.4 m ID \times 0.46 m L).

$$\gamma_0 = \gamma_{01} + \gamma_{02} \quad [A.5]$$

and the time to the limiting friction condition is given by Eq. [A.2]. The sum of t_1 and t_2 yields the total time of a slump and the slumping frequency,

$$\frac{1}{S} = \frac{1}{60} \left[\frac{\gamma_{01} + \gamma_{02}}{6 \cdot n} \right] + (C_1 + C_2) + C_3 \cdot n \quad [A.6]$$

To verify the regression coefficients obtained from the t_1 and t_2 data, the slumping frequency data¹ were regressed using Eq. [A.6], thus yielding an independent set of coefficients.

NOMENCLATURE

a Initial acceleration of shear wedge, m/s^2
 d_p Particle diameter, mm
 g Gravitational acceleration, m/s^2
 n Rotational speed of the cylinder, rpm
 n_c Critical rotational speed of the cylinder
 s Distance traveled by bulk solids in the shear wedge, m
 t Time, s
 t_0 Time required to traverse the limiting shear wedge
 t_1 Time from minimum to maximum bed inclination
 t_2 Time from maximum to minimum bed inclination
 v Linear velocity, m/s
 v_0 Initial granule velocity in its parabolic trajectory, m/s
 \bar{x}_{ABC} Abscissa of the centroid of the upper wedge, m
 \bar{x}_{PSC} Abscissa of the centroid of the lower wedge, m
 \bar{y}_{ABC} Ordinate of the centroid of the upper wedge, m
 \bar{y}_{PSC} Ordinate of the centroid of the lower wedge, m
 A Cross-sectional area of solids bed, m^2

C_1 Regression coefficient from curve fit on t_1 data, s
 C_2 Regression coefficient from curve fit on t_2 data, s
 C_3 Regression coefficient from curve fit on t_2 data, $60 \text{ s}^2/\text{rev}$
 D Cylinder diameter, m
 F_c Centrifugal force, N
 F_f Frictional force, N
 F_G Gravity force, N
 F_N Normal force, N
 F_R Resultant force, N
 F'_R Reaction force, N
 Fr Froude number ($\omega^2 R/g$)
 H Depth of the bulk solids in the rotary vessel, m
 J Pct filling, pct
 K Constant in Eq. [45] by Oyama⁷
 M Total mass of bulk solids in the rotary cylinder, kg
 R Inside radius of cylinder, m
 R_B Radius of rotation of the center of gravity of the bulk solids
 S Slumping frequency, slumps per minute
 X Abscissa of parabolic trajectory of particles, m
 X_E Abscissa of the midpoint of the bed surface, m
 Y Ordinate of parabolic trajectory of granules, m
 Y_E Ordinate of the midpoint of the bed surface, m
 β Angle relating the friction force and the normal force in the force balance on a slipping bed, deg
 γ Wedge angle, deg
 γ_0 Limiting shear wedge angle, deg
 γ_1 Wedge angle determined from Eq. [A1], deg
 γ_{01} Regression constant from curve fit on t_1 data, deg
 γ_{02} Regression constant from curve fit on t_2 data, deg
 γ^* Angle traversed by rotary cylinder in time t , deg
 η Slope of average trajectory of the shear wedge, deg

θ	Angle between the apex of the bed and the abscissa, deg
λ	Angular measure of the pct fill, deg
μ_D	Dynamic coefficient of friction of bulk solids
μ_L	Shearing coefficient of friction of bulk solids
$\mu_{W/S}$	Coefficient of friction between the cylinder wall and the bulk solids
ϕ'	Resultant angle of bed inclination for the force balance on a slipping bed, deg
ϕ_D	Dynamic angle of repose of bulk solids, deg
ϕ_L	Shear angle or lower angle of repose
ϕ_S	Angle of slipping friction
ϕ_U	Upper angle of repose
ϕ_D'	Resultant angle of bed inclination for the force balance on a cascading bed
ω	Angular velocity of the rotary cylinder, rad per second
$\omega_{R/C}$	Rotational speed at the rolling-cascading boundary, rad per second

ACKNOWLEDGMENTS

The authors are grateful to Stelco, Inc. and the Natural Sciences and Engineering Research Council of Canada for providing financial support in the form of a Stelco Fellowship and Research Assistantship, respectively. Appreciation is also expressed to Mr. E. Sunnergren of Bethlehem Steel, Mr. E. Whitlock of Domtar Chemicals Ltd., and Mr. W. Zimmer of Kennedy Van Saun Corporation for their help and cooperation during the various stages of this project.

REFERENCES

1. H. Henein, J. K. Brimacombe, and A. P. Watkinson: *Metall. Trans. B*, 1983, vol. 14B, pp. 191-205.
2. W. Schnabel: Ph.D. Thesis, Rheinisch-Westfälischen Technischen Hochschule Aachen, 1977.
3. R. Hogg: Ph.D. Thesis, University of California, Berkeley, CA, 1970.
4. J. Lehmberg, M. Hehl, and K. Schügerl: *Powder Tech.*, 1977, vol. 18, pp. 149-63.
5. K. W. Carley-Macaulay and M. B. Donald: *Chem. Eng. Sci.*, 1962, vol. 17, pp. 493-506.
6. K. W. Carley-Macaulay and M. B. Donald: *Chem. Eng. Sci.*, 1964, vol. 19, pp. 191-99.
7. Y. Oyama: *Rikwagaku-Kenkyo-Jo-Iho Bull.*, 1935, vol. 14, pp. 570-83.
8. J. B. Gayle and J. H. Gary: *Industrial and Engineering Chemistry*, 1960, vol. 52, pp. 519-20.
9. P. M. C. Lacey: *J. Appl. Chem.*, 1954, vol. 4, pp. 257-68.
10. P. V. Danckwerts: *Research*, 1953, vol. 6, p. 355.
11. C. W. Clump: "Mixing of Solids," chapter 10, vol. 2, J. B. Gray and V. W. Uhl, eds., *Mixing: Theory and Practices*, Academic Press, New York, NY, 1966/67.
12. R. Hogg: *Int. Conf. in Part. Technol.*, 1st Int. Inst. of Technol. Res. Inst., IIT Res. Inst., Chicago, IL, 1973, pp. 157-64.
13. H. Taubman: *Aufbereitungstechn.*, 1963, vol. 4, pp. 139-50.
14. W. R. Uggle: *Revue des Matériaux de Construction et de Travaux Publics*, 1930, ed. C, pp. 447-53.
15. J. J. Ronco: *Industria y Quimica*, 1960, vol. 20, pp. 605-14.
16. J. J. Ronco and M. de Santiago: Universidad Nacional de La Plata, Laboratorio de Ensayo de Materiales e Investigaciones Tecnológicas de la Provincia de Buen Aires (LEMIT), La Plata, República Argentina, unpublished research, 1959.
17. E. I. Khodorov: *The Movement of Material in Rotary Kilns*, Moscow, 1957.
18. G. von Halbart and V. Freymann: *Zement-Kalk-Gips*, 1960, vol. 13, pp. 17-23.
19. G. Reuter: Ph.D. Thesis, Rheinisch-Westfälischen Technischen Hochschule Aachen, 1975.
20. M. Cross: Report No. GS/TECH/553/1/74/C, British Steel Corp., London, U.K., 1974.
21. M. Cross: *Powder Technology*, 1979, vol. 22, pp. 187-90.
22. H. Henein: Ph.D. Thesis, The University of British Columbia, Vancouver, Canada, 1981.
23. E. W. Davis: *Trans. AIME*, 1919, vol. 61, pp. 250-96.
24. G. G. Eichholz: Investigation Report IR 59-25, Mines Branch, Ottawa, Canada, 1959.
25. H. E. Rose and R. M. E. Sullivan: *A Treatise on the Internal Mechanics of Ball, Tube and Rod Mills*, Constable and Company Ltd., London, 1957.
26. R. Rutgers: *Chem. Eng. Sci.*, 1965, vol. 20, pp. 1079-87.
27. W. D. Duda: *Cement-Data-Book*, 2nd ed., Macdonald & Evans, London, 1977, pp. 111-21 and pp. 319-26.
28. A. M. Gow, A. B. Campbell, and W. H. Coghill: *Trans. AIME*, 1930, vol. 87, pp. 51-81.
29. C. E. Sunnergren: Bethlehem Steel Corporation, Bethlehem, PA, 1979, National Lime Association Operators Meeting, Seattle, WA, 1979.
30. W. Zimmer: K. V. S. Corporation, Danville, PA, private communications, 1979.
31. E. Whitlock: Lime Division, Domtar Chemical Ltd., Montreal, Canada, private communications, 1979.
32. H. E. Rose and G. D. Blunt: *Proc. Instn. Mech. Engrs.*, 1956, vol. 170, p. 793.
33. V. I. Korotich: *Stal in English*, 1961, vol. 8, pp. 554-60.
34. R. E. Johnstone and M. W. Thring: *Pilot Plants, Models and Scale-up Methods in Chemical Engineering*, 1975, McGraw-Hill Book Co., New York, NY, pp. 226-32.
35. V. K. Darra and D. W. Fuerstenau: *Powder Technology*, 1977, vol. 16, pp. 97-105.
36. Fr. Muller: *Aufbereitungs-Technik*, 1966, vol. 5, pp. 274-85.